Research Article | Vol. 8, No. 7 | 1 Jul 2017 | BIOMEDICAL OPTICS EXPRESS 3143
Biomedical Optics EXPRESS

Measuring the effect of a Western diet on liver tissue architecture by FLIM autofluorescence and harmonic generation microscopy

SUMAN RANJIT,[1] ALEXANDER DVORNIKOV,[1] EVGENIA DOBRINSKIKH,[2] XIAOXIN WANG,[2] YUHUAN LUO,[2] MOSHE LEVI,[2] AND ENRICO GRATTON[1,*]

[1]*Laboratory for Fluorescence Dynamics, Department of Biomedical Engineering, University of California, Irvine, CA, USA*
[2]*Departments of Medicine, University of Colorado-Anschutz Medical Campus, Aurora, Colorado, USA*
[*]*egratton22@gmail.com*

Abstract: The phasor approach to auto-fluorescence lifetime imaging was used to identify and characterize a long lifetime species (LLS) (~7.8 ns) in livers of mice fed with a Western diet. The size of the areas containing this LLS species depends on the type of diet and the size distribution shows Western diet has much larger LLS sizes. Combination of third harmonic generation images with FLIM identified the LLS species with fat droplets and the droplet size distribution was estimated. Second harmonic generation microscopy combined with phasor FLIM shows that there is an increase in fibrosis with a Western diet. A new decomposition in three components of the phasor plot shows that a Western diet is correlated with a higher fraction of free NADH, signifying more reducing condition and more glycolytic condition. Multiparametric analysis of phasor distribution shows that from the distribution of phasor points, a Western diet fed versus a low fat diet fed samples of mice livers can be separated. The phasor approach for the analysis of FLIM images of autofluorescence in liver specimens can result in discovery of new fluorescent species and then these new fluorescent species can help assess tissue architecture. Finally integrating FLIM and second and third harmonic analysis provides a measure of the advancement of fibrosis as an effect of diet.

OCIS codes: (170.2520) Fluorescence microscopy; (100.0100) Image processing; (170.3650) Lifetime-based sensing.

References and links

1. Q. M. Anstee, G. Targher, and C. P. Day, "Progression of NAFLD to diabetes mellitus, cardiovascular disease or cirrhosis," Nat. Rev. Gastroenterol. Hepatol. **10**(6), 330–344 (2013).
2. G. Musso, R. Gambino, M. Cassader, and G. Pagano, "Meta-analysis: natural history of non-alcoholic fatty liver disease (NAFLD) and diagnostic accuracy of non-invasive tests for liver disease severity," Ann. Med. **43**(8), 617–649 (2011).
3. M. Yoneda, M. Yoneda, H. Mawatari, K. Fujita, H. Endo, H. Iida, Y. Nozaki, K. Yonemitsu, T. Higurashi, H. Takahashi, N. Kobayashi, H. Kirikoshi, Y. Abe, M. Inamori, K. Kubota, S. Saito, M. Tamano, H. Hiraishi, S. Maeyama, N. Yamaguchi, S. Togo, and A. Nakajima, "Noninvasive assessment of liver fibrosis by measurement of stiffness in patients with nonalcoholic fatty liver disease (NAFLD)," Dig. Liver Dis. **40**(5), 371–378 (2008).
4. P. Uhl, G. Fricker, U. Haberkorn, and W. Mier, "Current Status in the Therapy of Liver Diseases," Int. J. Mol. Sci. **15**(5), 7500–7512 (2014).
5. H. K. Hussain, "Imaging methods for screening of hepatic steatosis," in Clinical Dilemmas in Non-Alcoholic Fatty Liver Disease(John Wiley & Sons, Ltd), pp. 138–151 (2016).
6. P. Morelli, E. Porazzi, M. Ruspini, U. Restelli, and G. Banfi, "Analysis of errors in histology by root cause analysis: a pilot study," J. Prev. Med. Hyg. **54**(2), 90–96 (2013).
7. R. Vuppalanchi and N. Chalasani, "Nonalcoholic fatty liver disease and nonalcoholic steatohepatitis: Selected practical issues in their evaluation and management," Hepatology **49**(1), 306–317 (2009).
8. P. Greenspan, E. P. Mayer, and S. D. Fowler, "Nile red: a selective fluorescent stain for intracellular lipid droplets," J. Cell Biol. **100**(3), 965–973 (1985).
9. A. Mehlem, C. E. Hagberg, L. Muhl, U. Eriksson, and A. Falkevall, "Imaging of neutral lipids by oil red O for analyzing the metabolic status in health and disease," Nat. Protoc. **8**(6), 1149–1154 (2013).
10. A. C. Croce and G. Bottiroli, "Autofluorescence spectroscopy and imaging: a tool for biomedical research and diagnosis," Eur. J. Histochem. **58**(4), 2461 (2014).
11. A. C. Croce, U. De Simone, I. Freitas, E. Boncompagni, D. Neri, U. Cillo, and G. Bottiroli, "Human liver autofluorescence: an intrinsic tissue parameter discriminating normal and diseased conditions," Lasers Surg. Med. **42**(5), 371–378 (2010).

#291497 https://doi.org/10.1364/BOE.8.003143
Journal © 2017 Received 27 Mar 2017; revised 13 May 2017; accepted 19 May 2017; published 1 Jun 2017

Biomedical Optics EXPRESS

12. A. C. Croce, U. De Simone, M. Vairetti, A. Ferrigno, E. Boncompagni, I. Freitas, and G. Bottiroli, "Liver autofluorescence properties in animal model under altered nutritional conditions," Photochem. Photobiol. Sci. **7**(9), 1046–1053 (2008).
13. A. C. Croce, A. Ferrigno, L. G. Di Pasqua, C. Berardo, V. M. Piccolini, V. Bertone, G. Bottiroli, and M. Vairetti, "Autofluorescence discrimination of metabolic fingerprint in nutritional and genetic fatty liver models," J. Photochem. Photobiol. B **164**, 13–20 (2016).
14. A. C. Croce, A. Ferrigno, G. Santin, V. M. Piccolini, G. Bottiroli, and M. Vairetti, "Autofluorescence of liver tissue and bile: organ functionality monitoring during ischemia and reoxygenation," Lasers Surg. Med. **46**(5), 412–421 (2014).
15. M. Goetz, R. Kiesslich, H. P. Dienes, U. Drebber, E. Murr, A. Hoffman, S. Kanzler, P. R. Galle, P. Delaney, and M. F. Neurath, "In vivo confocal laser endomicroscopy of the human liver: a novel method for assessing liver microarchitecture in real time," Endoscopy **40**(7), 554–562 (2008).
16. M. Goetz, M. Vieth, S. Kanzler, P. R. Galle, P. Delaney, M. F. Neurath, and R. Kiesslich, "In vivo confocal laser laparoscopy allows real time subsurface microscopy in animal models of liver disease," J. Hepatol. **48**(1), 91–97 (2008).
17. H. Wang, X. Liang, Y. H. Mohammed, J. A. Thomas, K. R. Bridle, C. A. Thorling, J. E. Grice, Z. P. Xu, X. Liu, D. H. G. Crawford, and M. S. Roberts, "Real-time histology in liver disease using multiphoton microscopy with fluorescence lifetime imaging," Biomed. Opt. Express **6**(3), 780–792 (2015).
18. C. Arnesano, Y. Santoro, and E. Gratton, "Digital parallel frequency-domain spectroscopy for tissue imaging," J. Biomed. Opt. **17**(9), 096014 (2012).
19. C. A. Thorling, X. Liu, F. J. Burczynski, L. M. Fletcher, G. C. Gobe, and M. S. Roberts, "Multiphoton microscopy can visualize zonal damage and decreased cellular metabolic activity in hepatic ischemia-reperfusion injury in rats," J. Biomed. Opt. **16**(11), 116011 (2011).
20. M. Digman and E. Gratton, "The phasor approach to fluorescence lifetime imaging: Exploiting phasor linear properties," in *Fluorescence Lifetime Spectroscopy and Imaging* (CRC Press), pp. 235–248 (2014).
21. D. M. J. Enrico Gratton, "Phasor Approach to Fluorescence Lifetime Imaging Microscopy," (2017), http://www.lumipedia.org/index.php?title=Phasor_Approach_to_Fluorescence_Lifetime_Imaging_Microscopy2017.
22. R. Datta, A. Alfonso-García, R. Cinco, and E. Gratton, "Fluorescence lifetime imaging of endogenous biomarker of oxidative stress," Sci. Rep. **5**(1), 9848 (2015).
23. R. Datta, C. Heylman, S. C. George, and E. Gratton, "Label-free imaging of metabolism and oxidative stress in human induced pluripotent stem cell-derived cardiomyocytes," Biomed. Opt. Express **7**(5), 1690–1701 (2016).
24. V. Crosignani, A. Dvornikov, J. S. Aguilar, C. Stringari, R. Edwards, W. W. Mantulin, and E. Gratton, "Deep tissue fluorescence imaging and in vivo biological applications," J. Biomed. Opt. **17**(11), 116023 (2012).
25. V. Crosignani, S. Jahid, A. S. Dvornikov, and E. Gratton, "A deep tissue fluorescence imaging system with enhanced SHG detection capabilities," Microsc. Res. Tech. **77**(5), 368–373 (2014).
26. A. Dvornikov and E. Gratton, "Imaging in turbid media: a transmission detector gives 2-3 order of magnitude enhanced sensitivity compared to epi-detection schemes," Biomed. Opt. Express **7**(9), 3747–3755 (2016).
27. D. Débarre, W. Supatto, A.-M. Pena, A. Fabre, T. Tordjmann, L. Combettes, M.-C. Schanne-Klein, and E. Beaurepaire, "Imaging lipid bodies in cells and tissues using third-harmonic generation microscopy," Nat. Methods **3**(1), 47–53 (2006).
28. L. Gailhouste, Y. Le Grand, C. Odin, D. Guyader, B. Turlin, F. Ezan, Y. Désille, T. Guilbert, A. Bessard, C. Frémin, N. Theret, and G. Baffet, "Fibrillar collagen scoring by second harmonic microscopy: a new tool in the assessment of liver fibrosis," J. Hepatol. **52**(3), 398–406 (2010).
29. S. Ranjit, E. Dobrinskikh, J. Montford, A. Dvornikov, A. Lehman, D. J. Orlicky, R. Nemenoff, E. Gratton, M. Levi, and S. Furgeson, "Label-free fluorescence lifetime and second harmonic generation imaging microscopy improves quantification of experimental renal fibrosis," Kidney Int. **90**(5), 1123–1128 (2016).
30. S. Ranjit, A. Dvornikov, M. Levi, S. Furgeson, and E. Gratton, "Characterizing fibrosis in UUO mice model using multiparametric analysis of phasor distribution from FLIM images," Biomed. Opt. Express **7**(9), 3519–3530 (2016).
31. S. Ranjit, A. Dvornikov, M. Stakic, S.-H. Hong, M. Levi, R. M. Evans, and E. Gratton, "Imaging Fibrosis and Separating Collagens using Second Harmonic Generation and Phasor Approach to Fluorescence Lifetime Imaging," Sci. Rep. **5**(1), 13378 (2015).
32. M. Strupler, A. M. Pena, M. Hernest, P. L. Tharaux, J. L. Martin, E. Beaurepaire, and M. C. Schanne-Klein, "Second harmonic imaging and scoring of collagen in fibrotic tissues," Opt. Express **15**(7), 4054–4065 (2007).
33. M. A. Digman, V. R. Caiolfa, M. Zamai, and E. Gratton, "The Phasor Approach to Fluorescence Lifetime Imaging Analysis," Biophys. J. **94**(2), L14–L16 (2008).
34. N. G. James, J. A. Ross, M. Stefl, and D. M. Jameson, "Applications of Phasor Plots to in Vitro Protein Studies," Anal. Biochem. **410**(1), 70–76 (2011).
35. E. Brown, T. McKee, E. diTomaso, A. Pluen, B. Seed, Y. Boucher, and R. K. Jain, "Dynamic imaging of collagen and its modulation in tumors in vivo using second-harmonic generation," Nat. Med. **9**(6), 796–801 (2003).
36. D. K. Bird, L. Yan, K. M. Vrotsos, K. W. Eliceiri, E. M. Vaughan, P. J. Keely, J. G. White, and N. Ramanujam, "Metabolic Mapping of MCF10A Human Breast Cells via Multiphoton Fluorescence Lifetime Imaging of the Coenzyme NADH," Cancer Res. **65**(19), 8766–8773 (2005).
37. C. Stringari, A. Cinquin, O. Cinquin, M. A. Digman, P. J. Donovan, and E. Gratton, "Phasor approach to fluorescence lifetime microscopy distinguishes different metabolic states of germ cells in a live tissue," Proc. Natl. Acad. Sci. U.S.A. **108**(33), 13582–13587 (2011).

Biomedical Optics EXPRESS

1. Introduction

Non-alcoholic fatty liver disease (NAFLD) is a common pathological condition and results in high morbidity. NAFLD can cause wide sets of diseases associated with damaged liver, including steatosis, fibrosis, cirrhosis and can cause whole organ failure and morbidity [1–3]. NAFLD is usually imaged with Ultrasound, CT or MRI [4–6]. To estimate the extent of the damage and effectiveness of the treatment, often biopsies are carried out and stained and imaged by trained pathologists. Traditional histological techniques for liver biopsy imaging and analysis involve tissue staining with dyes specific for specific constituents and then optical imaging [5, 6]. A second imaging technique often employed is immunofluorescence microscopy [7]. Both of these techniques have some drawbacks. Histological techniques have the problem of differential sensitivities of dyes towards separate areas of the image, including heterogeneous binding affinity, non-specific binding and are dependent on pathologist's interpretation. Often multiple pathologists examine the same tissue section to remove operator bias [6]. The long tissue preparation time and dependency on pathologists makes this process time consuming. Immunofluorescence has the added difficulty associated with the production of antibodies specific to different components of the tissue. These antibodies are usually very costly and time consuming to develop. The post processing of the tissue samples using dyes or antibodies makes the procedure slower and any type of automatic image analysis along with decrease in post processing of the tissue slices prior to imaging will make the procedure faster and operator independent.

In place of using a lipid soluble dye (e.g. Nile red, Oil Red O etc.) to stain lipid rich areas of the biopsy or tissue sections [8, 9], we propose using native autofluorescence from the tissue sections as a probe to measure lipid deposition in liver. Autofluorescence has recently been used for the imaging in liver and has been pioneered by a series of paper by Croce et al, where they used autofluorescence spectral signals for identifying liver pathology and composition [10–16]. A main difference in our approach in employing autofluorescence is that we use autofluorescence lifetime in addition to spectral information. Different autofluorescence species have different lifetimes although they can have undistinguishable spectra, and the lifetime can change depending on the fluorophore environment. Fluorescence lifetime can be used to quantify changes in tissue composition and changes in architecture and lipid deposition. Recent work by Wang et al [17] has used multiphoton microscopy with Fluorescence Lifetime Imaging (MPM-FLIM) for liver imaging. A difference from their approach is the instrumentation and method of data analysis. Wang et al use time correlated single photon counting (TCSPC) approach in the time domain and our approach is based on the phasor approach to FLIM in the frequency domain [17–19]. The phasor approach to frequency domain FLIM can better distinguish long lifetimes species compared to the TCSPC approach, while TCSPC is sensitive to short lifetimes [20, 21]. The phasor approach in conjunction with a with a new 3-component analysis introduced in this paper can better detect and quantify a long lifetime species (LLS ~7.8 ns) found in the fat droplets in liver tissues resulting from western diet. Previously, this long lifetime species has been observed in cells fed with oleic acid or when the cells are under hypoxia to produce reactive oxygen species (ROS) or in the mouse adipose tissues [22, 23]. Raman signature for triglycerides is coincident with presence of this LLS species in these droplets under oleic acid treatment [22]. ROS oxidation of fat molecules is the probable cause for the formation of the LLS and here we have used this LLS signal to identify and distinguish the effect of western diet on liver tissue sections.

The microscope used for our measurements is based on a forward direction detector where the data is acquired in the direction of excitation and it is exquisitely sensitive for harmonic imaging [24–26]. In the work described in this paper, we have used third harmonic generation imaging which is especially sensitive to fat droplet boundaries to show that the LLS component coincides with the droplets [27]. We have also used a combinatorial approach of FLIM and second harmonic generation (SHG) to quantify the extent of fibrosis in the liver tissues [28–32].

Biomedical Optics EXPRESS

The analysis of FLIM by the phasor approach is very fast as it does not involve fitting of the decay to multi-exponentials at each pixel of the image [33]. Calculation of parameters from the phasor mapped FLIM images and the use of SHG to quantify and score fibrosis is a method of analysis that can be easily automated and this analysis could become pathologist independent [29]. In this paper, combination of the long lifetime species with the harmonic generation results in detecting the effect of western diet on liver morphology and fibrosis. Furthermore, using the law of phasor addition and a novel 3-species decomposition analysis allowed us to calculate the fraction of free/bound NADH when the phasor location of NADH is affected by the LLS component. Finally, the shape of the phasor distribution in each sample is a fingerprint of the abundance and species present in the FLIM image. The position and shape of the phasor distribution can be used to differentiate low fat diet liver samples from western diet liver samples and to calculate the extent of changes in the liver autofluorescence signature due to the variation in diet [30]. The multiparametric analysis of phasor distribution calculates the shape and position of the phasor distribution in multiple levels and then these parameters can be used to distinguish between different types of phasor distributions. The difference between samples can be quantified and the receiver operating curve (ROC) and the corresponding statistical parameters are estimated [30]. The phasor approach detects the presence of a long fluorescence lifetime species that can be used to quantify the changes in liver architecture. The combination of FLIM with harmonic generation results in quantification of fibrosis.

2. Methods

2.1 Animal model and tissue slice preparation

8-week-old C57BL/6J male mice were obtained from Jackson Labs. They were fed a matched control low fat diet (LF, 10 kcal% fat) or a western diet (WD, 42 kcal% milkfat, 34% sucrose, 0.2% cholesterol) for 6 months. Animal studies and relative protocols were approved by the Animal Care and Use Committee at the University of Colorado Denver. All animal experimentation was conducted in accordance with the Guide for Care and Use of Laboratory Animals (National Institutes of Health, Bethesda, MD).

At the end of the feeding period mice were anesthetized and livers were removed and processed frozen in OCT (Optimal Cutting Temperature) compound or formalin fixed and paraffin embedded (FFPE). The tissue was sliced in 5 µm thick sections and this section was mounted on a slide. The OCT compound was removed using DPBS buffer (ThermoFisher Scientific, Waltham, MA) and the slice was mounted on a coverslip using the same buffer. Paraffin slices were imaged with optical sectioning after "backing" slides at 60°C without further removing of paraffin with xylene and ethanol.

2.2 Data acquisition: DIVER and phasor approach to FLIM

The autofluorescence of liver sections (5 µm thick) was imaged using the homebuilt DIVER (Deep Imaging via Enhanced Recovery) microscope [24–26]. The freshly frozen tissue samples were originally embedded in OCT. The OCT compound was removed by using DPBS buffer (ThermoFisher Scientific, Waltham, MA) and then the samples were mounted on a coverslip (No. 1.5, ThermoFisher Scientific, Waltham, MA) using the same buffer. The SHG imaging involved formalin fixed paraffin embedded (FFPE) tissues, which were imaged with optical sectioning without removing paraffin. The DIVER is a homebuilt modified microscope based on an upright configuration. The details of this microscope have been described elsewhere [25, 30, 31]. Briefly, this microscope uses a forward detection scheme, which is ideally suited for harmonic generation imaging [29]. The large area photon counting detector of the DIVER is connected to a FAST-FLIM unit (ISS, Champaign, IL), which can acquire the fluorescence decay at each pixel of the image. For fluorescence decay and SHG images the samples were excited with the 710 nm wavelength of a DeepSee Insight laser (Spectra-Physics, Santa Clara, CA) using a 40 X 0.8 NA water objective (Olympus, Waltham, MA). To acquire the third harmonic generation signal, samples were excited with 1050 nm

Biomedical Optics EXPRESS

using the same 40x objective. The sample was placed on top of the detector assembly consisting of the housing with filter wheel and large area PMT. An index matching liquid in the microscope optical path from the sample to the detector prevents loss of photons by reflection. The signal from the tissue sample is passed through the filter wheel and is collected by the PMT in the direction of excitation. Two BG39 filters create the incoming and outgoing window of the filter assembly and prevent the excitation laser hitting the detector. A combination of UG11 and BG39 filters creates a window of observation around 350 nm and is used for separating both SHG and THG [29]. A different filter was used to separate the blue wavelength (400 – 500 nm) and used for FLIM imaging. We note that a very small amount of tissue autofluorescence leaks into the SHG filter. This is very useful since it allows us to calculate the ratio between SHG and autofluorescence form the position of the phasor along the line of linear combination of autofluorescence and SHG. The signal acquired by the PMT is transferred to the phasor plot using the FAST-FLIM box. The images were taken with a field of view of 360 µm. Zoomed-in images were measured for FOV 90 µm. The pixel dwell time was 32 µs and each image was scanned 16 times to increase S/N.

2.3 Data analysis

2.3.1 Phasor analysis

The fluorescence and harmonic signals collected from each point of the image was transformed to the Phasor Space using the following transformation [20, 33, 34]

$$s_{i,j}(n\omega)=\frac{\int_0^T I_{i,j}(t)\sin(n\omega t)dt}{\int_0^T I_{i,j}(t)dt},\ g_{i,j}(n\omega)=\frac{\int_0^T I_{i,j}(t)\cos(n\omega t)dt}{\int_0^T I_{i,j}(t)dt} \quad (1)$$

where, $s_{i,j}(\omega)$ and $g_{i,j}(\omega)$ are the Y and X coordinates in the phasor plot, respectively; ω is the repetition frequency of the laser source in radians, T is the period of the laser repetition frequency and n is the harmonic frequency. $I_{i,j}$ is the intensity decay measured at each pixel in the original optical image. The fluorescence collected from every pixel of an image is transformed to a point in the phasor plot. Changes in the metabolism and lipid accumulation due to changes in the diet can change the position of the phasor points and the overall distribution pattern of the phasor plot. A set of phasor points can then be chosen using a colored cursor and the corresponding image can be colored accordingly. We describe multiple different ways to analyze the phasor distribution to quantify different species in the tissue under observation.

2.3.2 Calculation of the size of the lipid droplets

The location of long lifetime species in the phasor plot was selected with the red cursor and the FLIM images were colored accordingly (Fig. 1(d)). The LLS species is only present in the lipid droplets. Thus, the size of the droplets can be measured by measuring the size of the area of the images covered by LLS. There are a large number of very small size droplets which are usually present in liver tissues. A thresholding of >85 μm^2 in the size distribution for the fat droplets results in better separation of the images from the liver tissues of high fat western diet and low fat control diet. The droplet sizes can then be represented by a box plot or by histograms (Fig. 1(e) and 1(f). The box plot shows how the average and standard deviation of the size of the droplets change based on the type of the diet. The histogram shows how the droplets for western diet extend to much larger sizes than that observed for the low-fat diet samples.

2.3.3 Calculation of fraction of free and bound NADH

The combination and location of the phasor components in the FLIM analysis is governed by the law of phasor addition [20]. According to this law, the position of a phasor point resulting

Biomedical Optics EXPRESS

from the fluorescence decay at a particular pixel of an image can be traced back to the phasor positions of the components responsible for fluorescence at that particular point. The law of phasor addition dictates that the relative contributions of two or more phasor points towards another point in between them are inversely proportional to the distances between the point in the middle and their corresponding phasor points [20]. The FLIM images for western diet liver have a phasor signature in the NADH channel that is a result of their original contributing species. The images taken with the NADH filter have contribution from free NADH (~0.4 ns), bound NADH (3.4 ns) and the long lifetime species (~8 ns). These three components were chosen with green, blue and red cursors, respectively in Fig. 2(a). The individual fractions can be calculated depending on the position of the phasor points inside the triangle determined by the red, green and blue cursors.

Given an experimental point of coordinates g and s (black dot, Fig. 2(a)), if only 3 species are present in a sample (free and bound NADH and LLS) the point must fall in the triangle with red, green and blue corners. Then the rule of phasor's addition was used to determine the relative amount of bound to free NADH and LLS fraction as follows. A line passing through the red and black dot was drawn and this line intercepted with the line between the green and blue dots. The intercept point is used to determine the relative concentration of bound to free using the ratio

$$\text{Fraction of free NADH} = \text{distance}(\text{intercept to blue})/\text{distance}(\text{green to blue}) \quad (2)$$

The fraction of LLS was obtained using the ratio

$$\text{LLS fraction} = \text{distance}(\text{point-to intercept})/\text{distance}(\text{intercept to red}) \quad (3)$$

We have used this decomposition to transform the distribution of phasor points to the distribution of free and bound NADH. The ratio of free to bound NADH is related to the ratio of NAD^+/NADH in the tissue and thus free to bound NADH distribution is a measure of changes in metabolism. After subtracting the effect of the LLS species, the true distribution of free to bound NADH from the western and low fat diet samples can be compared and the changes in the metabolism can be assessed.

2.3.4 Multiparametric analysis of phasor distribution

The distribution of phasor points originating from a FLIM image is a fingerprint of the image and is particular to the corresponding image. Difference in the phasor distribution between different sets of data is often distinguished by the changes in average position of the phasor points. However, often the average position is not enough to describe the changes in the phasor distribution. Previously we have developed a multiparametric approach for the analysis of the phasor distribution [30]. For the clarification of the analysis used in the paper this approach is described again below. First, the histogram in the phasor distribution is divided in four equal heights based on the maximum height of the phasor distribution histogram. Then for each segment five parameters including average (g), average (s), the length (a) and width (b) of the distribution (considering it as ellipse) and the angle of the distribution (θ) is calculated based on the spatial moment of the distribution.

The spatial moment of the distribution was calculated from the individual phasor point positions:

$$M_{ij} = \frac{\sum_g \sum_s g^i \cdot s^j \cdot I(g,s)}{\sum_g \sum_s I(g,s)} \quad (4)$$

where, $I(g,s)$ is the value of the phasor histogram at position g and s. The central moment is then calculated using the following relation:

Biomedical Optics EXPRESS

$$\mu_{pq} = \sum_{g}\sum_{s}\left(g-\bar{g}\right)^{p}\cdot\left(s-\bar{s}\right)^{q} f(g,s) \tag{5}$$

where, *p, q*, and *f(g,s)* are the indices indicating the rank of the moment, respectively. This analysis uses moments up to rank 2.

The angle is calculated using:

$$\theta = \frac{1}{2}\arctan\left(\frac{2\mu'_{11}}{\mu'_{20}-\mu'_{02}}\right) \tag{6}$$

Finally, the shape of the distribution is calculated from value of the major (*a*) and minor axis (*b*):

$$a,b = \frac{\mu'_{20}+\mu'_{02}}{2} \pm \frac{\sqrt{4\mu'^{2}_{11}+(\mu'_{20}-\mu'_{02})^{2}}}{2} \tag{7}$$

Then these multiple parameters were combined to create a spectrum that corresponds to that particular phasor distribution. Finally, the two different sets of phasor distributions belonging to the western diet and low fat liver images are compared by adding a set of fitting parameters for each of the components. Once the value of these fitting parameters are determined for the best separation between the western diet and low fat diet, receiver operating characteristic curve (ROC curve was calculated and various statistical parameters, including the area under the curve (AUC value), true and false positive rates, sensitivity and positive prediction rate can be calculated and the different tissue samples can be compared [30]. The data presented here used the parameters *g, s, a, b* for the comparison.

2.3.5 Third harmonic generation microscopy

Third harmonic generation results from the abrupt changes in the refractive index at the tissue boundaries. In this process the emitted light is of one-third wavelength compared to the excitation wavelength. In tissues, there is a large change of refractive index at the boundary of lipid droplets and these droplets generate a strong THG signal [27]. In this paper THG have been used to show that the LLS species in FLIM images overlaps with the lipid droplets. This is specifically shown for the zoomed-in images for low fat diet liver, where the zoomed images show that these small LLS spots actually belongs to lipid droplets.

2.3.6 Imaging fibrosis with second harmonic generation

Second harmonic generation (SHG) in tissue and biological systems is specifically sensitive to fibrillary collagens and myelin [28, 31, 32, 35]. SHG is a nonlinear optical process, which is generated when a light of wavelength (λ) interacts with a non-centrosymmetric fibrillary structure (e.g., collagen I) and a signal at half of the incident wavelength (λ/2) is generated. Fibrosis is associated with an increase in the collagen content, specifically the non-centrosymmetric collagen fibers. SHG microscopy has been widely used to study the extent of fibrosis in tissue samples. In a recent study, we have used the ratio of areas covered by SHG to the ratio of areas covered by autofluorescence and used this ratio to quantify fibrosis. We have used the same methodology here to study the extent of fibrosis as a result of changes in diet. The SHG signal is coherent, resembles that of the laser pulse, has a lifetime of zero, and appears at s = 0, g = 1 coordinates of the phasor plot. The autofluorescence that can bleed through for the 710 nm excitation has a non-zero lifetime and appears inside the universal circle of the phasor plot. The SHG signal and FLIM signal was selected with green and red cursors, respectively, and the area in the corresponding image was colored accordingly. The area covered by green to red (f_{green}/f_{red}) was used as a measure of extent of fibrosis [29]. This method ensures that the changes in the tissue architecture is combined with increasing SHG and gives a better measure of the extent of fibrosis compared to just the calculation of the amount of SHG alone.

Biomedical Optics EXPRESS

3. Results

3.1 Size of the droplet calculation

The fluorescence intensity images are shown in Fig. 1(a). These FLIM images were color mapped (Fig. 1(b)) after the long lifetime species (LLS) in the phasor plot was selected with the red cursor (Fig. 1(d)). A comparison between these color-coded FLIM images and the third harmonic images (Fig. 1(c)) show that the LLS actually overlaps with the THG signal, proving that the LLS species are present in the lipid droplets. The samples with low fat diet (LF) were zoomed-in (FOV 90 µm) to show that the LLS is actually coincident with the THG signal. Figure 1(b) shows representative FLIM images from western and low fat diet, respectively. This comparison also shows that the sizes of the droplets are much larger for the western diet mice. A size comparison using a histogram and a boxplot are also shown (Fig. 1(e), 1f). The boxplot clearly shows that the average sizes of the lipid droplets are much larger than the droplets sizes of the low-fat diet mice. The histograms show that the fat droplets have an overall large size distribution. However, the larger droplets are only present for the western diet mice. The averages of eight images for six animals are plotted in Fig. 1(e) and the standard deviation of the images was used for the boxplot.

3.2 3-component phasor analysis

The western diet also affects the metabolism in the liver. The change in the metabolism is related to the change in the ratio of NAD+/NADH. However, it has been shown that the metabolic ratio of NAD+/NADH is related to the ratio of free to protein bound NADH [36]. NAD + is non-fluorescent but NADH is fluorescent. Free NADH has a lifetime of 0.4 ns and when bound to enzymes, for example Lactate dehydrogenase (LDH), has a lifetime of 3.4 ns [22]. Spectral analysis shows that the LLS species cannot be separated from the emission of NADH so we must exploit the differences in decay time alone. However, the presence of the LLS species moves the position of the pixel with different ratios of free/bound NADH toward the LLS location in the phasor plot due to the rule of linear combination. Therefore, we need to decompose the relative contribution of each species at each pixel. This is a huge problem when using the decomposition of the decay in exponentials but it reduces to a simple graphical construction using the phasor representation and the rule of phasor addition for 3 species. As shown in Fig. 2(a) the position of the bound and free NADH species is shown with the cursors green and blue, respectively. The position of the LLS species is shown with the red cursors. The line joining bound and free NADH is called metabolic trajectory. In terms of metabolism a move toward the freer NADH (blue cursor) is representative of a more reducing condition and a glycolytic metabolism; while a move towards more bound NADH (green cursor) is representative of more oxidizing conditions and more oxidative phosphorylation [37]. Figure 2(b) shows the fractional component of the phasor distribution projected along the axis of bound to free NADH based on the three-component decomposition analysis described in the Methods section. The lines in Fig. 2(b) show that the distributions display a larger fraction of free NADH in the western diet mice samples and thus fat diet introduces more reducing condition. The distribution of LLS component shows that the percentage of LLS is larger for the western diet mice sample (Fig. 2(c)).

Biomedical Optics EXPRESS

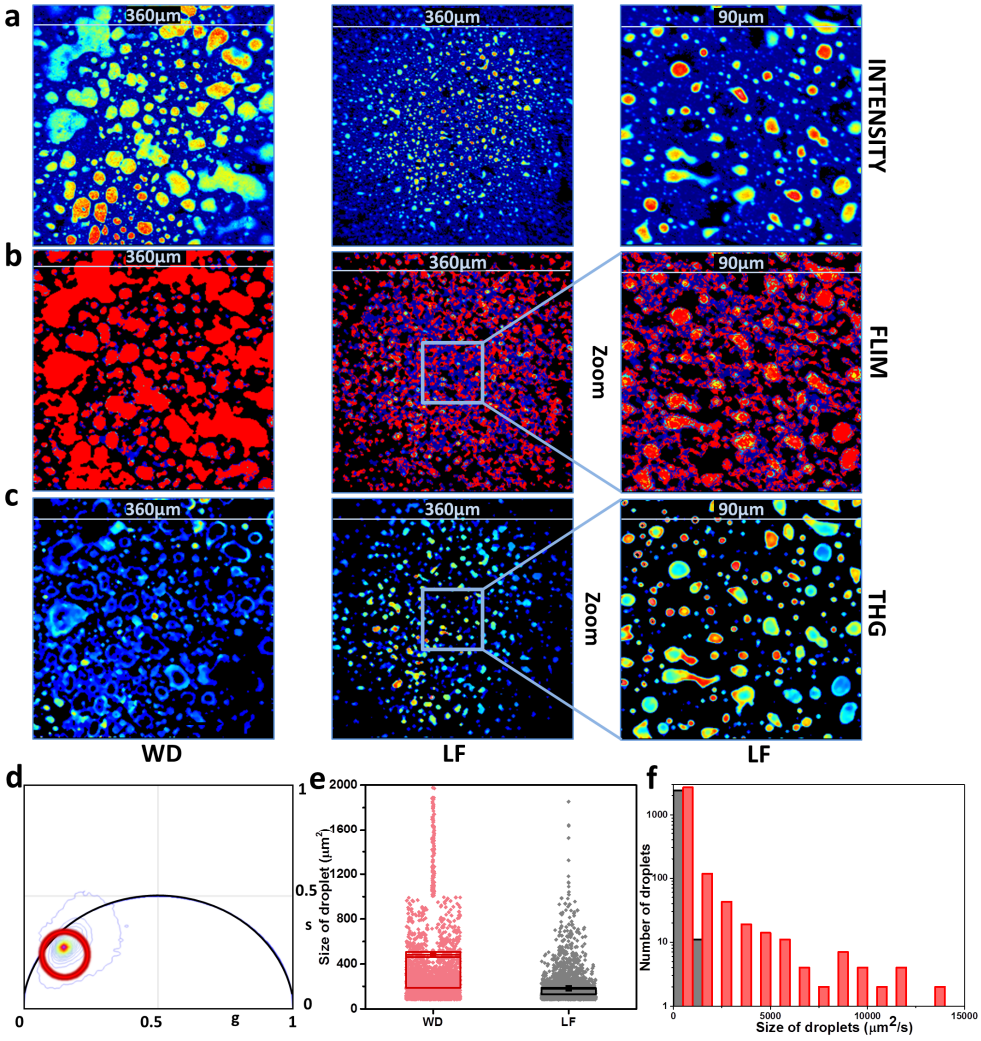

Fig. 1. Effect of diet on the size of lipid droplets. (a) Representative fluorescence intensity images, (b) autofluorescence FLIM images and (c) third harmonic generation (THG) images from fat diet (WD) and nonfat diet (LF) samples, respectively. The FOV is 360 µm. Zoomed in images (90µm) (right panel) of intensity (a) FLIM (b) and THG (c) shows that LLS signals from LF diet mice liver tissue samples are coincident with very small droplets. These images are taken by zooming into the corresponding LF (360 µm) images. (d) Phasor plot of the liver FLIM images. The red cursor was used to select the long lifetime species (LLS) in the phasor plot and the FLIM images were colored accordingly with phasors selected by the red course. (e) Boxplot describing the average (small filled square) and standard deviation (top and bottom of the box) for WD (red) and LF (black) samples. The dots represent individual measurement from each image. (f) Histogram of droplet sizes above 85 µm^2. Red and grey represent WD and LF samples, respectively. The p value for the Kolmogorov-Smirnov (K-S) test for the data in panel e and f was smaller than 0.0001.

Biomedical Optics EXPRESS

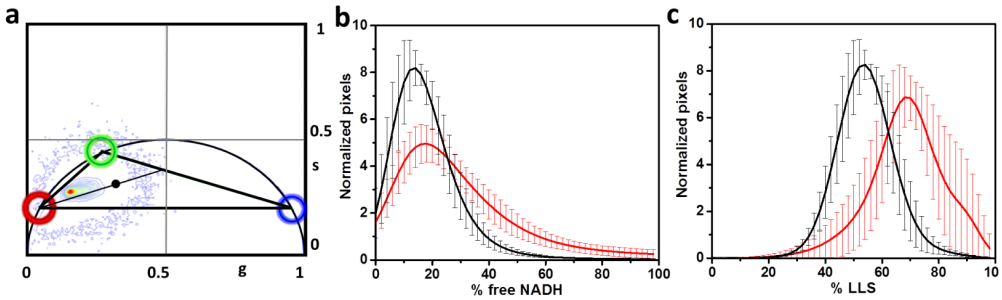

Fig. 2. Decomposition of the phasor plot using three components (a) The location of three components in the phasor distribution used for separating the various contributions are shown and red, green and blue representing LLS, bound and free NADH, respectively. The black point represents a point in the phasor distribution whose fraction is mapped using the equations described in the Methods section. (b) Changes in the fraction of free NADH and (c) fraction of LLS species for the low fat (black) and western (red) diet, respectively. The error bars in panels b and c correspond to the standard deviation of 9 independent samples for each diet condition and the continuous lines correspond to the average of the 9 independent samples for each condition.

3.3 Multiparametric analysis

The multiparametric separation index using the phasor distribution as the fingerprint of the tissue images are shown in Fig. 3(a). The parameters used for the separation included average *g, s, a, b*. Figure 3(a) shows the separation between the low-fat (black) and western diet (red) mice samples. In this method, best separation is achieved when the red points are not overlapping with dark gray points; the separation is very good and the degree of the separation can be seen from the Area Under the Curve (Fig. 3(b)) which is 1.0. The high AUC value determines the separation achieved by analysis of the shape of phasor plot between diets and this is conveyed by the following statistical parameters including accuracy (0.98), specificity (0.97), sensitivity (1.00), positive prediction value (0.96) and true/false positive rate (1.00/0.03).

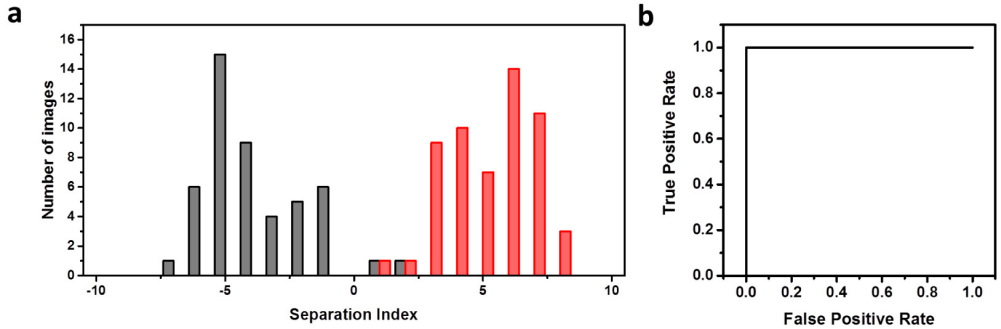

Fig. 3. (a) Separation of low fat and western diet images using multiparametric approach. Black and red represent low fat and western diet, respectively. (b) ROC analysis with an AUC of one showing the complete separation achieved by the multiparametric approach.

3.4 Second harmonic generation analysis

The results from the SHG imaging are presented in Fig. 4. The intensity images from western diet (WD and low fat (LF) diet are shown in Fig. 4(a). These images were then color-coded using a green color for the centrosymmetric collagen fiber and a red color for bleed through autofluorescence (Fig. 4(b)). The SHG signal is coherent and resembles the laser pulse and has a lifetime of zero. It appears at s = 0, g = 1 in the phasor plot (Fig. 4c) and this was selected with a green cursor. The autofluorescence resulting from the 710 nm excitation can bleed through the filters for the SHG channel. However, this autofluorescence have a nonzero lifetime, appears within the universal circle of the phasor plot, and was selected with a red

Biomedical Optics EXPRESS

cursor. The color-coded images according to the color of the cursor are shown in Fig. 3(a), where the not centrosymmetric collagen fiber signal was colored green and the autofluorescence was colored red. The ratios of the fraction of area covered by green to red (f_{green}/f_{red}) are plotted in Fig. 4d. This ratio determines the amount of non-centrosymmetric collagen accumulation in the image and accounts for changes in the tissue architecture [29]. The averages of eight images for six animals are plotted in Fig. 4d and the standard error of mean amongst the animals was used as the error bar. The data shows that there is a correlation of fibrosis with the diet and the extent of fibrosis increases with increasing fat-sucrose-cholesterol (western diet) in diet. This data shows how a combination of SHG and autofluorescence can be used together to quantify fibrosis and measure the effect of diet on collagen accumulation.

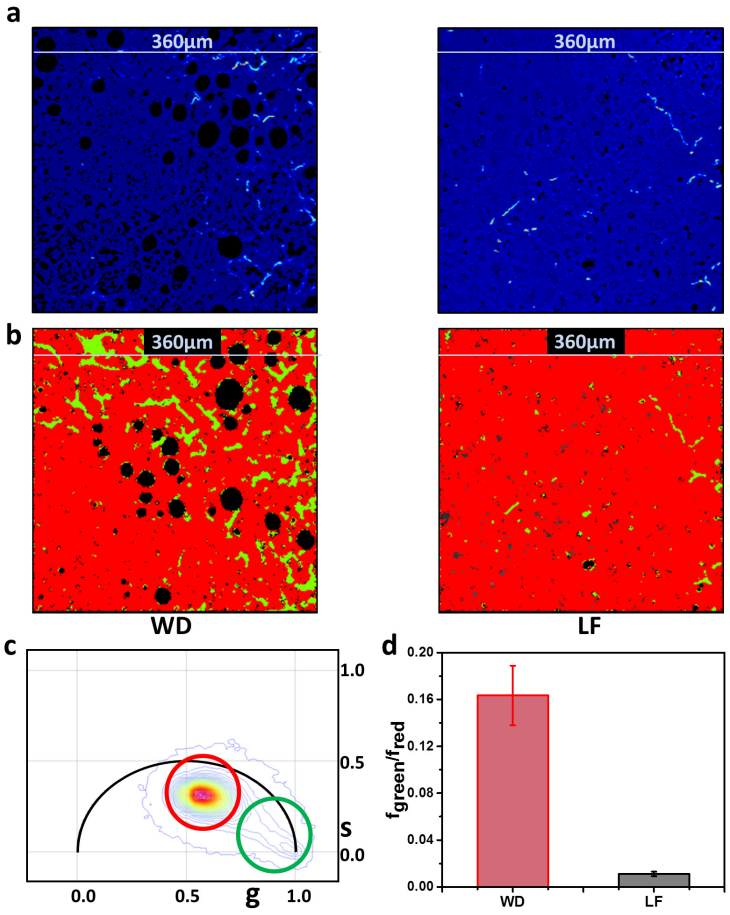

Fig. 4. Imaging and quantification of fibrosis in mouse liver as a function of diet. (a) Intensity images in the SHG channel and (b) Color coded images of liver tissues from WD and LF mice are shown according to the cursor selection in (c). The green colors show region of the image displaying SHG generation from collagen I and the red shows bleed-through autofluorescence originating from rest of the tissue. Black spots are regions lacking autofluorescence. This is due to the paraffin sectioning of these tissues where the fat droplet gets dissolved in the paraffin. The signal from LLS is absent in these images and appear as black holes. (c) Phasor plot used to separate the coherent SHG signal (green cursor, lifetime of zero) and the bleed-through autofluorescence (red cursor, non-zero lifetime) and color the FLIM images accordingly. (d) The ratio of the area covered by SHG (f_{green}) (green) to the area covered by bleed through autofluorescence (red, f_{red}). The higher value of the ratio correlates with advanced fibrosis. The average over all animals is presented here with the standard error of the mean as the error bar. Six animals of each type were measured and eight images were measured for each animal. The p value for the paired sample t-test for panel d was less than 0.0001.

Biomedical Optics EXPRESS

4. Discussion

Diet induced changes in the liver architecture have been previously studied by histology and fluorescence imaging. In this paper, we have introduced the phasor approach to autofluorescence FLIM to measure the effect of NAFLD. The use of FLIM images and the phasor approach provides identification of a long lifetime species that is present in the fat droplets. The origin of this long lifetime species is unknown. However, these species have been observed in brown adipose tissues, cells under influence of oleic acid or under the presence of reactive oxygen species (ROS). The presence of this species is related to the oxidation of lipids and one of the components of this LLS species is believed to be lipid oxidation product. The value of this long lifetime species is ~7.8 ns. Selection of regions of the images where the LLS is present was used to calculate the size of the lipid droplets and to measure the effect of fat diet on tissue architecture. The FLIM images acquired in the blue channel show a combination of 3 species in each pixel. The three-component decomposition of phasor distribution shows that fatty diet results in freer NADH and a change of metabolism to more glycolytic and reducing condition. The amount of increase in fat can also be quantified. The multiparametric analysis of phasor histogram shows that the type of diet results in significant changes of shape of the phasor distribution. The multiparametric combinatorial approach shows that phasor signatures originating from the two sets of samples from mice of the two diets are substantially different and multiparametric analysis achieves complete separation of western diet samples from low -fat diet with a very high specificity and a very high true positive rate. Combining SHG with FLIM and phasor approach can result in easy separation of non-centrosymmetric collagen fibers in the tissue and directly correlate the increase in fibrosis with increasing fat intake. The biological significance of this study in calorie restriction and diet induced obesity, inflammation and NASH is of high significance. However, the main effort of this paper is directed towards introducing a quantitative analysis method based on FLIM images and the phasor analysis of these images. We show that the combination of phasor-FLIM approach can result in the discovery of new lifetime species, (e.g. the long lifetime species or LLS here) and exploiting this new autofluorescent species for the quantification of liver tissue architecture under diet change. FLIM autofluorescence with the phasor approach results in detecting changes in tissue architecture without histological staining and results in analysis pipelines which are pathologist independent and computationally automatable. In conclusion, combining FLIM with phasor analysis enables quantitative description of tissue composition, metabolism, and indicates a pipeline for automatic tissue analysis.

Funding

National Institutes of Health ((NIH)-P41 GM103540, NIH-P50 GM076516, VAMR 1I01BX001954, NIH 1R01DK098336 and NIH 1R01AG049493); Intercept Pharmaceuticals (205069).

Acknowledgment

National Institutes of Health (NIH)-P41 GM103540 and NIH-P50 GM076516 to E.G and S.R., VAMR 1I01BX001954, NIH 1R01DK098336 and NIH 1R01AG049493 to M.L, and Award No. 205069 from Intercept Pharmaceuticals to S.R.

We thank Milka Stakic for technical assistance.